Unveiling the mechanism of abnormal magnetic behavior of FeNiCoMnCu high-entropy alloys through a joint experimental-theoretical study

Ziyuan Rao,[1] Biswanath Dutta,[2] Fritz Körmann,[1,2] Dirk Ponge,[1] Linlin Li,[1] Junyang He,[1] Leigh Stephenson,[1] Lukas Schäfer,[3] Konstantin Skokov,[3] Oliver Gutfleisch,[3] Dierk Raabe,[1] and Zhiming Li[1,4,*]

[1]*Max-Planck-Institut für Eisenforschung GmbH, Max-Planck-Straße 1, 40237 Düsseldorf, Germany*

[2]*Materials Science and Engineering, Delft University of Technology, Mekeleweg 2, 2628 CD Delft, The Netherlands*

[3]*Institut für Materialwissenschaft, Technische Universität Darmstadt, Alarich-Weiss-Straße 16, 64287 Darmstadt, Germany*

[4]*School of Materials Science and Engineering, Central South University, 410083 Changsha, China*

(Received 7 September 2019; published 10 January 2020)

We combined experimental investigations and theoretical calculations to unveil an abnormal magnetic behavior caused by addition of the nonmagnetic element Cu in face-centered-cubic FeNiCoMn-based high-entropy alloys (HEAs). Upon Cu addition, the probed HEAs show an increase of both Curie temperature and saturation magnetization in as-cast and homogenized states. Specifically, the saturation magnetization of the as-cast HEAs at room temperature increases by 77% and 177% at a Cu content of 11 and 20 at. %, respectively, compared to the as-cast equiatomic FeNiCoMn HEA without Cu. The increase in saturation magnetization of the as-cast HEAs is associated with the formation of an Fe-Co rich phase in the dendritic regions. For the homogenized HEAs, the magnetic state at room temperature transforms from paramagnetism to ferromagnetism after 20 at. % Cu addition. The increase of the saturation magnetization and Curie temperature cannot be adequately explained by the formation of Cu enriched zones according to atom probe tomography analysis. *Ab initio* calculations suggest Cu plays a pivotal role in the stabilization of a ferromagnetic ordering of Fe, and reveal an increase of the Curie temperature caused by Cu addition which agrees well with the experimental results. The underlying mechanism behind this phenomenon lies in a combined change in unit-cell volume and chemical composition and the related energetic stabilization of the magnetic ordering upon Cu alloying as revealed by theoretical calculations. Thus, the work unveils the mechanisms responsible for the Cu effect on the magnetic properties of FeNiCoMn HEAs, and suggests that nonmagnetic elements are also crucial to tune and improve magnetic properties of HEAs.

DOI: 10.1103/PhysRevMaterials.4.014402

I. INTRODUCTION

In recent years a different type of alloys containing multiple principal elements, termed high-entropy alloys (HEAs), have been proposed [1,2]. The HEA concept provides access to a large composition spectrum of new alloys some of which show good mechanical, physical, and chemical properties [3–11]. The mechanical properties of HEAs have been extensively studied [12–17] but their functional properties are less explored. Most recent studies on functional properties of HEAs have addressed thermal, electrical, and magnetic properties, yet detailed studies on the underlying mechanisms are still rare [18–26]. While as an example for specific functional properties the resistive and superconducting properties of a TaNbHfZrTi HEA with a critical temperature of 7.3 K have been addressed [20], long term benefits could arise from HEAs with combinations of good mechanical and functional properties.

The magnetic properties are one of the most promising functional features of HEAs [17,19,21,22,27,28]. Several FeCoNi-based HEAs have been reported to show excellent magnetic properties [19,24,27,29]. For instance, $FeCoNi(AlSi)_{0.2}$ has a good combination of saturation magnetization, electrical resistivity, and malleability [19], a profile that might be suited for certain soft magnetic applications. However, the saturation magnetization values of most HEAs are lower than those of conventional magnetic materials [19,24,27,28]. This is due to the fact that nonmagnetic elements (e.g., Al, Si) in HEAs tend to decrease their saturation magnetization, a problem affecting soft and hard magnetic materials which should both have high saturation magnetization. Thus, identifying elements which can keep or even increase the saturation magnetization of HEAs is thus of importance. In this regard, the influences of most elements on saturation magnetization of HEAs are, however, still unclear.

The influence of Cu on the magnetism of transition metals has long been studied. Among the 3*d* transition metals, only Fe, Ni, and Co are ferromagnetic while Mn is antiferromagnetic in bulk form. It is reasonable to speculate that the addition of nonmagnetic Cu to magnetic alloys would in principle lead to a reduction of the saturation magnetization and Curie temperature. Indeed, both the saturation magnetization and Curie temperature decrease monotonically with increasing Cu content in Ni-Cu, Co-Cu, and Fe-Cu alloys [30–32]. However, the impact could be in principle different from this linear phenomenological rule if the alloys become compositionally

*Corresponding author: zhiming.li@mpie.de; lizhiming@csu.edu.cn

TABLE I. Bulk chemical compositions of the three as-cast HEAs in atomic percent measured by inductively coupled plasma mass spectrometry.

Alloys	Fe	Ni	Co	Mn	Cu
$Fe_{25}Ni_{25}Co_{25}Mn_{25}$	25.1	24.9	25.0	25.0	
$Fe_{22.2}Ni_{22.2}Co_{22.2}Mn_{22.2}Cu_{11.2}$	22.7	22.1	22.1	21.9	11.2
$Fe_{20}Ni_{20}Co_{20}Mn_{20}Cu_{20}$	20.2	20.0	20.0	19.9	19.9

so much more complex as for the case of HEAs and also if in addition further antiferromagnetic elements such as, e.g., Mn or Cr are involved.

In the present study, the equiatomic FeNiCoMn HEA matrix provides such a complex chemical environment for the study of the influence of Cu on the magnetic properties. Indeed we surprisingly observe here an abnormal increase of magnetization and Curie temperature after Cu addition to the FeNiCoMn-based HEA. Experimental techniques including atom probe tomography (APT) and theoretical methods such as density-functional theory (DFT) are combined to unveil the fundamental mechanisms responsible for this unusual magnetic phenomenon.

II. METHODOLOGY

A. Alloy processing

The ingots of the three HEAs, namely $Fe_{25}Ni_{25}Co_{25}Mn_{25}$, $Fe_{22.2}Ni_{22.2}Co_{22.2}Mn_{22.2}Cu_{11.2}$, and $Fe_{20}Ni_{20}Co_{20}Mn_{20}Cu_{20}$ (all in at. %) (denoted as FeNiCoMn, $FeNiCoMnCu_{0.5}$, and FeNiCoMnCu in the following context) with the same dimensions of $25 \times 60 \times 65$ mm^3 were cast in a vacuum induction furnace using pure metals (>99.8% purity). The as-cast samples were machined from the cast ingots. We used different temperatures to homogenize the HEAs due to their different thermal stabilities as the melting temperature of the HEA significantly as a function of the Cu content. For the equiatomic FeNiCoMn HEA without Cu, an as-cast alloy plate was hot-rolled at 900 °C to a thickness reduction of 50% (thickness reduced from 10 to 5 mm). The hot-rolling process allows us to eliminate the dendritic microstructure and potential casting defects [33]. After hot rolling, it was homogenized at 1200 °C for 2 h in Ar atmosphere followed by water quenching. For the other two HEAs containing Cu, namely $FeNiCoMnCu_{0.5}$ and equiatomic FeNiCoMnCu, alloy plates with the same dimensions were hot rolled at 600 °C to a 50% thickness reduction and homogenized at 1000 °C for 2 h. The bulk chemical compositions of the three as-cast HEAs were measured by inductively coupled plasma (ICP) mass spectrometry (Table I).

B. Microstructural characterization

The microstructures of the as-cast and homogenized HEAs were analyzed using multiple probing methods. X-ray diffraction (XRD) measurements were performed using an x-ray equipment ISODEBYEFLEX 3003 equipped with Co Kα ($\lambda = 1.788\,965$ Å) radiation operated at 40 kV and 30 mA. Backscattered electron imaging (BSEI) was performed on a Zeiss-Merlin instrument. Electron backscatter diffraction (EBSD) measurements of homogenized alloys were carried out on a Zeiss-Crossbeam XB 1540 FIB scanning electron microscope (SEM) with a Hikari camera and the TSL OIM software. The grain sizes in the homogenized alloys were calculated from multiple BSE images and EBSD maps by the intercept method. The elemental distributions in the as-cast and homogenized alloys were investigated using energy-dispersive x-ray spectroscopy (EDS) at microscale. The nanoscale elemental distributions in the homogenized alloys were investigated by atom probe tomography (APT) (LEAP 3000X HR, Cameca Inc.). Site-specific liftout of APT tips was performed from the homogenized alloys with a focused ion beam (FIB) instrument (FEI Helios Nanolab 600i) [34–36].

Prior to the microstructural analysis, fine polishing of the samples' surfaces was conducted using an oxide suspension (OPS) with silica particle sizes around 50 nm for more than 30 min to effectively remove the deformation layer caused by mechanical grinding. The sample surfaces were finally polished with soap and ethanol for 5 min to remove the nanosilica particles.

C. Magnetic property measurements

Temperature dependence of magnetization $M(T)_H$ of the as-cast and homogenized alloys were measured on rectangular shaped $3 \times 3 \times 1$ mm^3 samples using a Quantum Design Physical Properties Measurement System (PPMS 14) equipped with a standard vibrating sample magnetometry (VSM) option. The $M(T)_H$ dependence was measured at 0.01 and 1 T in a temperature range from 5 to 400 K. The temperature-sweeping rate was 1 K/min. Hysteresis loops $M(H)_T$ were taken at room temperature in an external magnetic field of ± 5 T using a LakeShore VSM Model 7410.

D. Density functional theory calculations

The total energy calculations were carried out using density functional theory (DFT) implemented in the exact muffin-tin orbital (EMTO) formalism [37,38]. The charges and the total energies were obtained within the generalized gradient approximation (GGA) parametrized by Perdew-Burke-Ernzerhof (PBE) [39]. The coherent potential approximation (CPA) [40] was used to treat chemical disorder in random alloys while the paramagnetic state was modeled by the disordered local moment (DLM) approximation [41]. The Monkhorst-Pack [42] scheme with a $30 \times 30 \times 30k$-point mesh was used for the Brillouin zone integration. The EMTO-CPA approach has been widely used in the past for investigating various HEAs and their properties [28,43,44].

III. RESULTS

A. Microstructure and compositional homogeneity

Figure 1 shows the XRD patterns of the as-cast and homogenized FeNiCoMn, $FeNiCoMnCu_{0.5}$, and FeNiCoMnCu HEAs. Both the as-cast FeNiCoMn and $FeNiCoMnCu_{0.5}$ show only one set of diffraction peaks, all pertaining to the face-centered-cubic (fcc) crystal structure. The XRD pattern of the as-cast FeNiCoMnCu has a sideband on the (220)

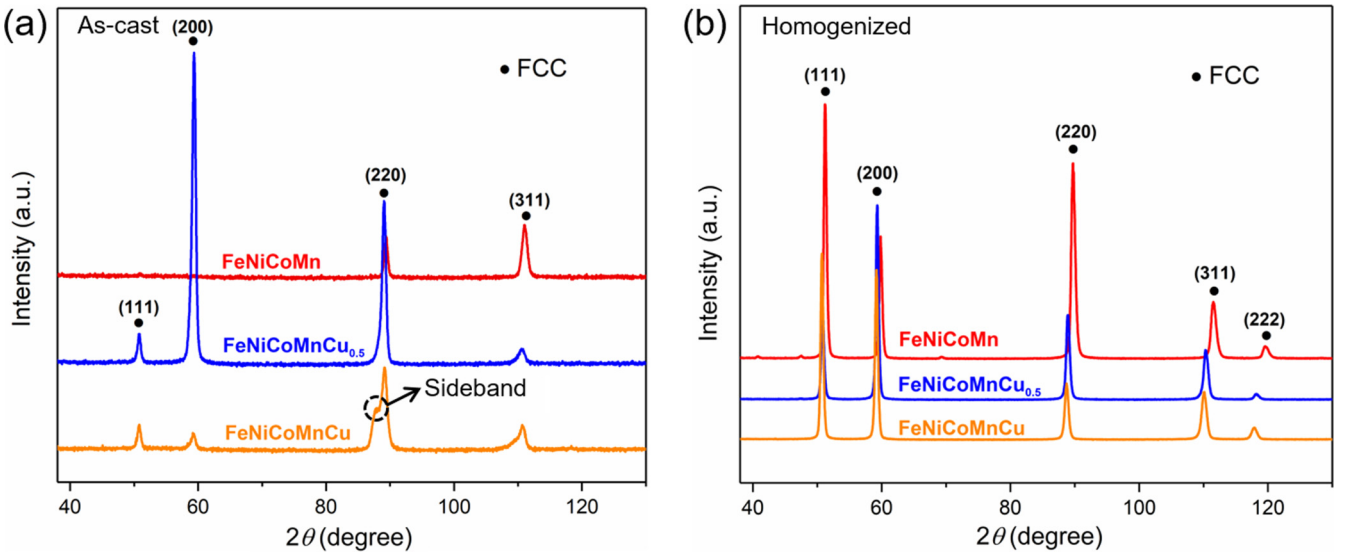

FIG. 1. XRD patterns of (a) as-cast and (b) homogenized FeNiCoMn, $FeNiCoMnCu_{0.5}$, and FeNiCoMnCu HEAs.

peak as marked by a dashed black circle in Fig. 1(a). The sideband indicates the existence of two fccphases with slightly different lattice parameters [45,46]. The lattice parameters of fccstructures in the as-cast FeNiCoMn and $FeNiCoMnCu_{0.5}$ HEAs are 0.36029 and 0.36030 nm, respectively. For the as-cast FeNiCoMnCu, the lattice parameter of the main fccphase and the secondary fccphase corresponding to the sideband are 0.36227 and 0.36638 nm, respectively. According to Fig. 1(b), all three HEAs mainly show a single fccstructure in a homogenized state. The diffraction peaks shift toward lower diffraction angles, suggesting the increase of the lattice parameter with increasing Cu concentration. The fcclattice parameters of the homogenized FeNiCoMn, $FeNiCoMnCu_{0.5}$, and FeNiCoMnCu HEAs are calculated from the XRD patterns as 0.358 90, 0.361 27, and 0.362 00 nm, respectively.

Figure 2 shows the BSE images with corresponding EDS maps of the as-cast FeNiCoMn, $FeNiCoMnCu_{0.5}$, and FeNiCoMnCu HEAs. Typical dendritic microstructures can be observed in all of the as-cast alloys. From Fig. 2(a), the dendrite regions are enriched with Fe and Co but depleted with Ni and Mn in the FeNiCoMn HEA. With the addition of Cu in $FeNiCoMnCu_{0.5}$ and FeNiCoMnCu HEAs, the interdendrite regions are enriched with Cu, Mn, and Ni, while Fe and Co are still enriched in the dendrite regions. From the EDS point analysis results listed in Table II, the Cu concentration in the interdendritic regions is 3.5 times that in the dendrite regions in $FeNiCoMnCu_{0.5}$. With more Cu added, the interdendrite regions are enriched with more Cu in FeNiCoMnCu. Combing the EDS and XRD results shows that the main fccphase in the as-cast FeNiCoMnCu is the dendrite phase enriched with Fe and Co, while the secondary fccphase is the interdendrite region enriched with Ni, Mn, and Cu.

Figures 3–5 show the EBSD maps, BSE images, EDS mapping, and line scan results of the homogenized FeNiCoMn,

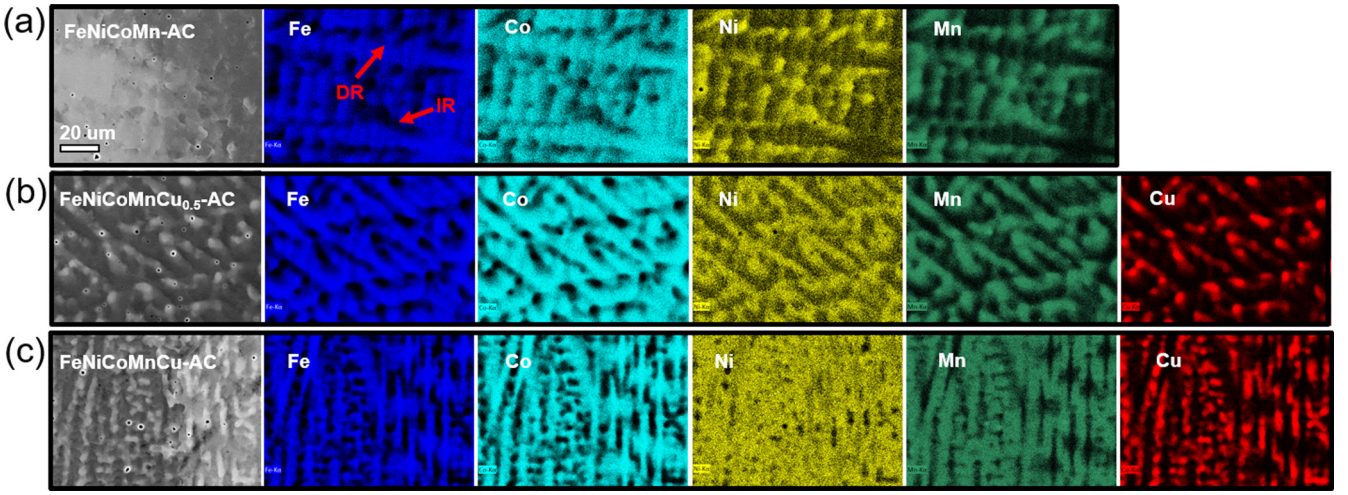

FIG. 2. BSE images and corresponding EDS maps of as-cast (AC) HEAs. (a) FeNiCoMn, (b) $FeNiCoMnCu_{0.5}$, (c) FeNiCoMnCu. All as-cast alloys show a typical dendritic microstructure. The dendrite (DR) and interdendrite (ID) regions are indicated by red arrows in the EDS map of Fe in (a).

TABLE II. Chemical compositions in the dendrite (DR) and interdendrite (ID) regions of the as-cast FeNiCoMn, $FeNiCoMnCu_{0.5}$, and FeNiCoMnCu HEAs obtained by EDS point analysis.

Alloy	Region	Fe (at. %)	Co (at. %)	Ni (at. %)	Mn (at. %)	Cu (at. %)
FeNiCoMn	DR	30.55	27.89	21.11	20.45	
	IR	24.20	24.40	24.63	26.77	
$FeNiCoMnCu_{0.5}$	DR	27.82	25.90	19.96	19.17	7.16
	IR	11.67	13.00	21.77	28.29	25.26
FeNiCoMnCu	DR	28.43	26.80	18.24	16.22	10.30
	IR	8.41	9.42	16.15	22.75	43.26

$FeNiCoMnCu_{0.5}$, and FeNiCoMnCu HEAs, respectively. The EBSD maps in Figs. 3(a) and 3(b), 4(a) and 4(b), and 5(a) and 5(b) show that all alloys are fully recrystallized with only single fccstructure. According to the calculation from multiple BSE images and EBSD maps, the average grain sizes of the homogenized FeNiCoMn, $FeNiCoMnCu_{0.5}$, and FeNiCoMnCu HEAs are ∼44.4, ∼10.5, and ∼ 9.78 μm (excluding annealing twin boundaries), respectively. FeNiCoMn has a four times larger grain size than the other two alloys because of the higher homogenization temperature (1200 °C). With increasing Cu content, the line fraction of twin boundaries decreases from 32% in FeNiCoMn to 22% in FeNiCoMnCu. Figures 3(b), 4(b), and 5(b) show the EDS maps of the homogenized FeNiCoMn, $FeNiCoMnCu_{0.5}$, and FeNiCoMnCu HEAs, respectively. All elements in the FeNiCoMn HEA are uniformly distributed [Figs. 3(b) and 3(c)]. From the line scan results shown in Figs. 4(c) and 5(c) for Cu containing HEAs, Cu is repelled by Fe and Co, while Mn and Ni are quite uniformly distributed. The inclusions which are mainly composed of Mn, O, and S are identified from the EDS line scan analysis as shown in Figs. 3(c) and 4(c).

B. Magnetic properties

Figure 6(a) shows the temperature-dependent magnetization curves for the homogenized FeNiCoMn, $FeNiCoMnCu_{0.5}$, and FeNiCoMnCu HEAs under an applied magnetic field of 1 T. An important observation here is the increase of the magnetization with increasing content of nonmagnetic Cu over almost the entire temperature range. Table III lists the values of saturation magnetization at room temperature determined from the hysteresis loops (see Fig. 14 in the Appendix) for the different alloys. It can be seen that only the homogenized equiatomic quinary FeNiCoMnCu HEA exhibits ferromagnetic behavior while the other two alloys are paramagnetic at room temperature. The as-cast alloys on the other hand exhibit typical features of soft magnetic materials with low coercivity for all three compositions. Similar to the homogenized alloys, these alloys also show higher saturation magnetization with higher Cu content.

The impact of Cu on the magnetic transition temperature is also depicted in Fig. 6(a), revealing that the transition shifts to higher temperatures for higher Cu content. The measured

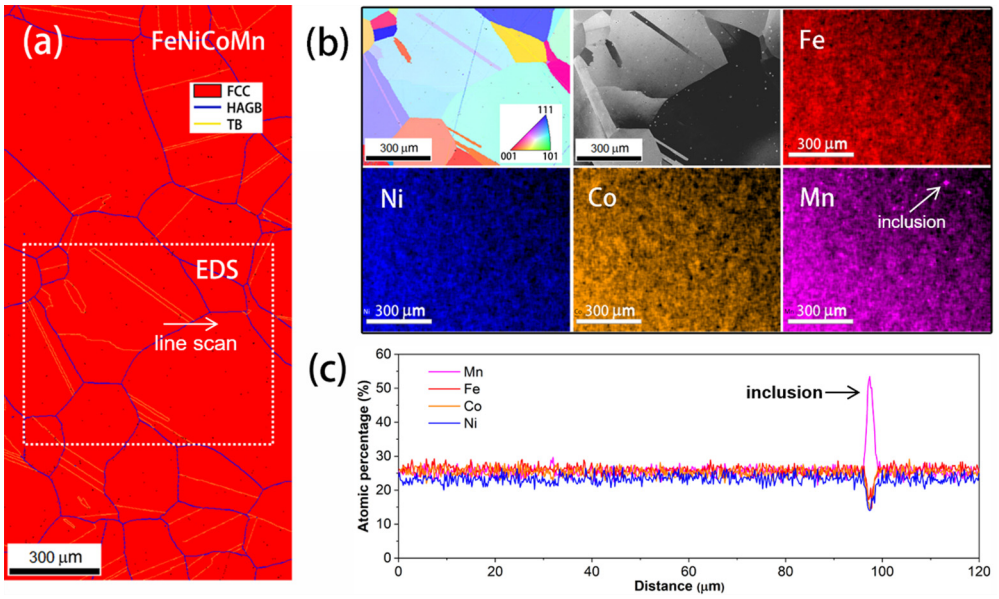

FIG. 3. Microstructure and elemental distribution of the homogenized FeNiCoMn HEA. (a) EBSD phase and boundary map; (b) EBSD IPF map, BSE image, and corresponding EDS maps of Fe, Ni, Co, and Mn with an identical sample region marked in (a). (c) EDS line scan analysis result of the area marked by the white arrow in (a).

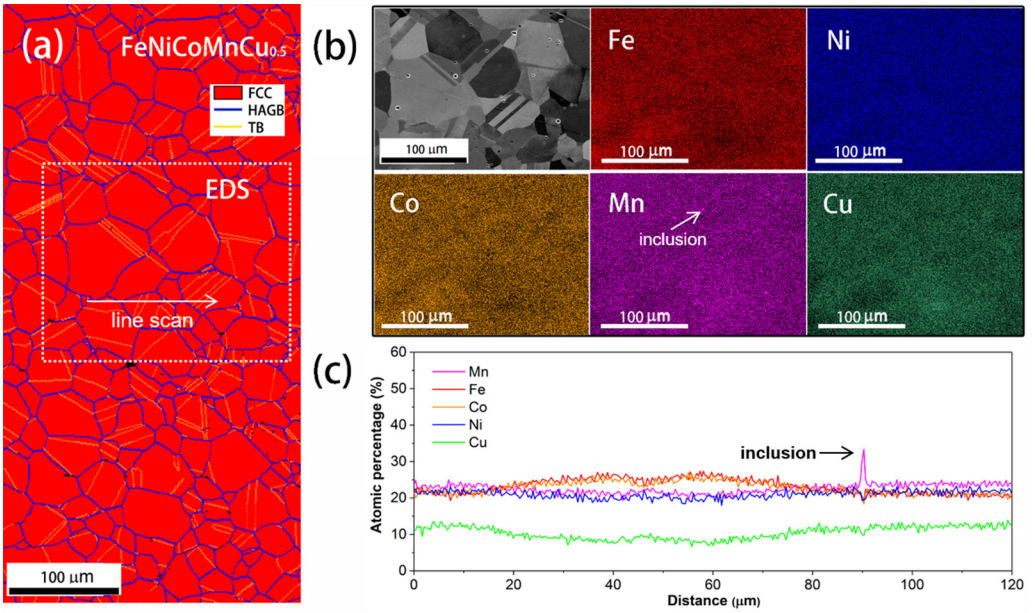

FIG. 4. Microstructure and elemental distribution of the homogenized $FeNiCoMnCu_{0.5}$ HEA. (a) EBSD phase and boundary map; (b) BSE image and corresponding EDS maps of Fe, Ni, Co, Mn, and Cu with an identical sample region marked in (a). (c) EDS line scan analysis result of the area marked by the white arrow in (a).

Curie temperatures from the demagnetization curves (see Fig. 15 in the Appendix) at low magnetic field of 0.01 T are listed in Table III. For the homogenized alloys, the Curie temperature increases monotonically with increasing Cu content. Only the quinary FeNiCoMnCu alloy, however, has a Curie temperature higher than room temperature (302 K) while the other two HEAs have Curie temperatures below room temperature (156 K for FeNiCoMn and 276 K for $FeNiCoMnCu_{0.5}$). This observation is in agreement with their corresponding magnetization values at room temperature. In contrast, in the as-cast condition FeNiCoMn has a similar Curie temperature as $FeNiCoMnCu_{0.5}$. When increasing the Cu content to 20 at. %, the FeNiCoMnCu HEA has a much higher Curie temperature (398 K) compared to the other two alloys. The Curie temperatures of all the as-cast HEAs are above room temperature.

The fundamental mechanisms responsible for these changes in the magnetic behavior with the increase of Cu content are discussed in the following, based on APT results and DFT calculations.

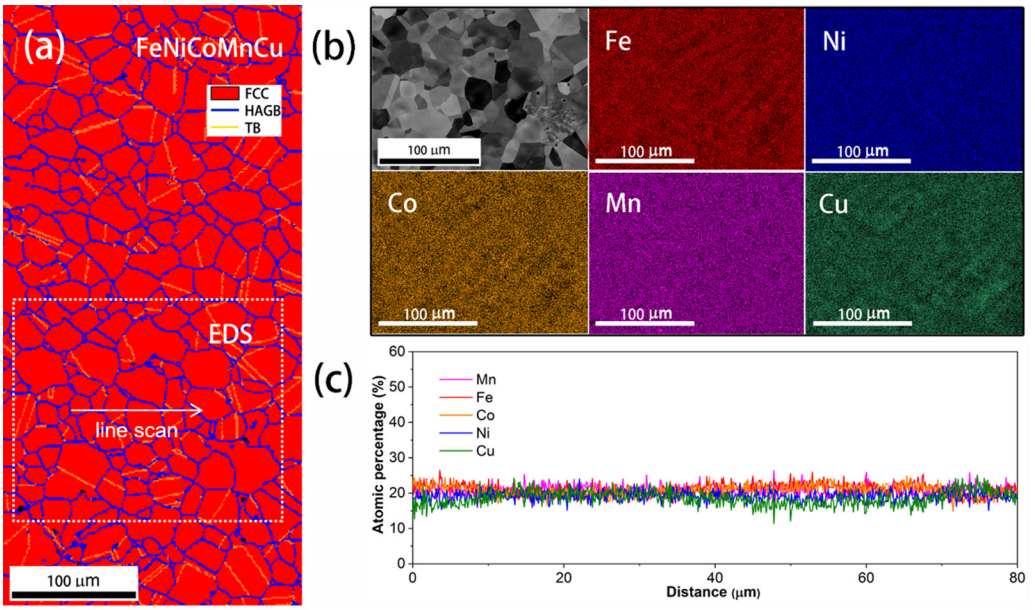

FIG. 5. Microstructure and elemental distribution of the homogenized FeNiCoMnCu HEA. (a) EBSD phase and boundary map; (b) BSE image and corresponding EDS maps of Fe, Ni, Co, Mn, and Cu with an identical sample region marked in (a). (c) EDS line scan analysis result of the area marked by the white arrow in (a).

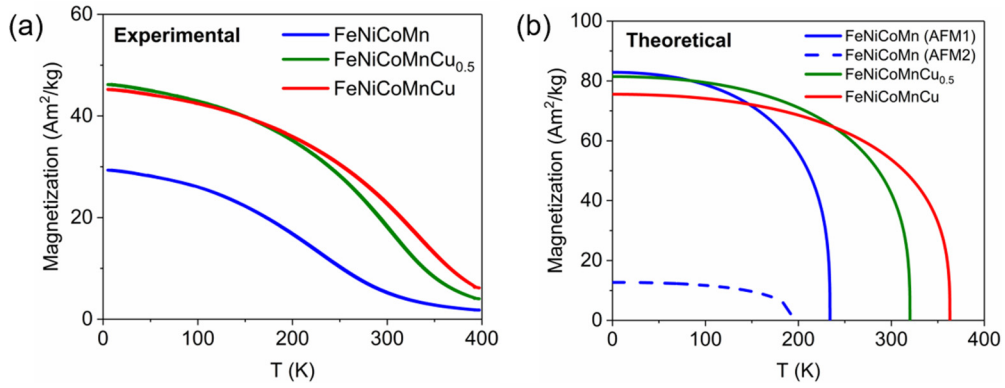

FIG. 6. Magnetization as a function of temperature for the homogenized FeNiCoMn, $FeNiCoMnCu_{0.5}$, and FeNiCoMnCu HEAs as obtained from (a) experimental measurements at a magnetic field of 1 T and (b) theoretical calculations. In the antiferromagnetic1 (AFM1) state (b), Mn atoms are arranged in alternating layers having up and down spins respectively with all Fe and Co spins aligned only in one direction. For the antiferromagnetic2 (AFM2) state, both Mn and Fe atoms have layered antiferromagnetic arrangement of spins while Co spins remain aligned in one direction alike AFM1 state (see Fig. 16). The values at 0 K are calculated using the exact muffin-tin–orbital coherent potential approximation (EMTO-CPA) approach while the complete temperature dependence is determined using the empirical Kuz'min formula [47,48].

IV. DISCUSSION

A. Effect of Fe-Co enriched phase in as-cast alloys

Compared to the homogenized alloys, the as-cast alloys have more complicated microstructures with the existence of dendrite and interdendrite phases. The formation of an Fe-Co enriched phase in the dendritic regions of the as-cast alloys becomes also apparent in the variation of the magnetic properties between the as-cast and homogenized alloys. In Fig. 7, we compare the Curie temperatures of the three alloys in the as-cast and homogenized states. The saturation magnetization is not included in this histogram because some alloys are paramagnetic at room temperature. The main trend is that the as-cast alloys show higher Curie temperatures than the homogenized alloys with identical bulk composition. This suggests that the Fe-Co enriched phase can increase the Curie temperature of the current alloy system. For instance, aging of FeCrCo hard magnetic alloys at ∼600 °C leads to formation of two phases, a ferromagnetic Fe-Co enriched phase and a nonmagnetic Cr enriched phase. This leads to a significant increase of saturation magnetization and Curie temperature of the material [49]. In Al-containing HEAs such as FeCoNiCrAl [50] and FeCoNiCrCuAl [4], Al addition causes a high degree of decomposition in Fe-Co enriched zones and then results in the increase of the saturation magnetization [18].

Further, for as-cast alloys with different Cu contents, the Curie temperature increases with the Cu content (Fig. 7). This coincides with the higher decomposition tendency observed for the alloys with higher Cu content. Specifically, as shown in Table II, the contents of Fe and Co in the dendrite phase of the FeNiCoMn alloy are about 3–6% higher than in the interdendrite phase. For the $FeNiCoMnCu_{0.5}$ alloy, the contents of Fe and Co in the dendrite phase are about twice that in the interdendrite phase. By further increasing the Cu content to the FeNiCoMnCu alloy, the Fe and Co contents in the dendrite phase are three times larger as compared to the interdendrite phase. However, it should be noted that the change of the Curie temperatures in the as-cast alloys with different Cu contents cannot be fully attributed to the effect of the Fe-Co enriched phase in the dendritic regions from the decomposition of the as-cast alloys. The intrinsic factors, e.g., the changes in volume and chemical composition caused by addition of Cu can also modulate the magnetic properties of as-cast alloys, as discussed below based on *ab initio* calculations in Sec. IV C by considering the ideal fcc solid solutions with homogeneous mixing of atoms.

For the homogenized alloys, the increase of the Curie temperature is also observed with the addition of Cu. However, only one fccphase can be detected by XRD and EBSD (Figs. 1 and 3–5). Although slight compositional fluctuations in the

TABLE III. Saturation magnetization and Curie temperature values obtained for the as-cast and homogenized FeNiCoMn, $FeNiCoMnCu_{0.5}$, and FeNiCoMnCu HEAs measured by vibrating sample magnetometry (VSM). The saturation magnetization is investigated up to 0.5 T at room temperature. The Curie temperature is measured by varying the temperature from 150 to 400 K at 0.01 T in vacuum and calculated by the derivative of the magnetization-temperature (M-T) curves.

Alloy	State	Room temperature saturation magnetization (A m^2/kg)	Curie temperature (K)
FeNiCoMn	as-cast	∼9	∼332
	homogenized		∼156
$FeNiCoMnCu_{0.5}$	as-cast	∼16	∼324
	homogenized		∼276
FeNiCoMnCu	as-cast	∼25	∼398
	homogenized	∼18	∼302

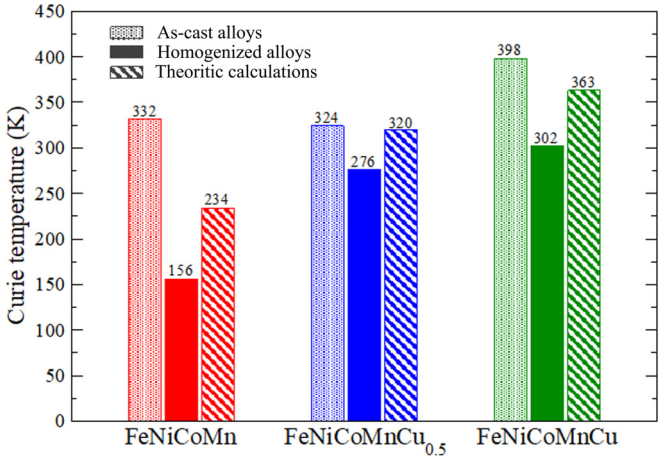

FIG. 7. Curie temperatures of as-cast and homogenized FeNiCoMn, $FeNiCoMnCu_{0.5}$, and FeNiCoMnCu HEAs. For the same bulk composition, the as-cast alloy has a higher Curie temperature than the homogenized alloy. The corresponding Curie temperatures obtained from theoretical calculations based on a mean-field approximation are also presented for comparison.

homogenized $FeNiCoMnCu_{0.5}$ and FeNiCoMnCu HEAs can be seen from the EDS line scan analysis [Figs. 3–5(c)], the fluctuation is too weak to identify possible decompositions. For this reason we performed further APT analysis to quantitatively identify the nanoscale elemental distribution in the homogenized alloys.

B. Nanoscale elemental distribution in homogenized alloys

Figure 8(a) shows the APT analysis of the nanoscale elemental distribution in the homogenized FeNiCoMn alloy. No apparent elemental segregation or decomposition can be observed in the 3D reconstructions at this length scale. From the statistical binomial frequency distribution analysis results shown in Fig. 8(b), all elements are uniformly distributed at the nanoscale. The values of the normalized homogenization parameter μ for all elements are close to 0, confirming the random distribution of all elements. The 1D compositional profile in Fig. 8(c) shows the same result. The tip has an overall composition of $Fe_{25.6}Ni_{26.5}Co_{25.4}Mn_{22.4}$ (all in at. %), matching the bulk composition obtained from wet-chemical analysis fairly. Combining the EDS mapping and line-scan analysis in Figs. 3(b) and 3(c), all elements in the homogenized FeNiCoMn HEA are uniformly distributed at both, micro- and nanoscale.

Figure 9(a) shows the results of the APT tip reconstructions for Fe, Ni, Co, Mn, and Cu in the homogenized $FeNiCoMnCu_{0.5}$ alloy. The 1D compositional profile in Fig. 9(b) shows slight elemental fluctuation, but no obvious segregation or decomposition. The tip has an overall composition of $Fe_{22.9}Ni_{23.9}Co_{22.7}Mn_{21.2}Cu_{9.2}$ (all in at. %), which acceptably matches the bulk composition. Figure 9(c) shows the radial distribution functions of Cu-Fe, -Co, -Ni, -Mn, and -Cu in the homogenized $FeNiCoMnCu_{0.5}$ alloy. This profile shows the probability density of finding an atom at 2 nm spacing when a Cu atom is placed at the origin [52,53] and 0.2 nm was taken as the step size as well as the shell thickness. The

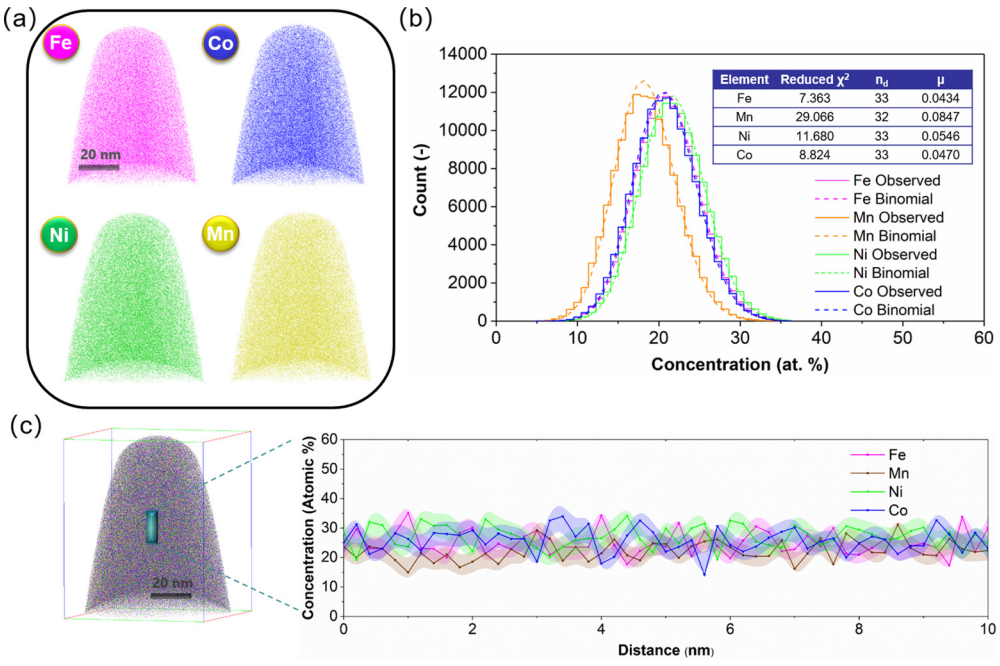

FIG. 8. APT analysis of the homogenized FeNiCoMn alloy. (a) 3D APT tip reconstructions of Fe, Ni, Co, and Mn. (b) Frequency distribution analysis obtained both from the observed experimental results and from the binomial simulation. The binomial simulation is a grid-based frequency distribution technique in which each voxel contains a constant total number of atoms [51]. Several parameters are employed to assess the quality of the fit of the experimental results to the binomial simulation, as listed in the inserted table. n_d is the number of degrees of freedom for a given ion, and μ is the normalized homogenization parameter. The values of the normalized homogenization parameter μ for all four elements are close to 0, indicating the random distribution of elements. (c) 1D compositional profile along the length direction of the cylinder shown in the 3D APT tip.

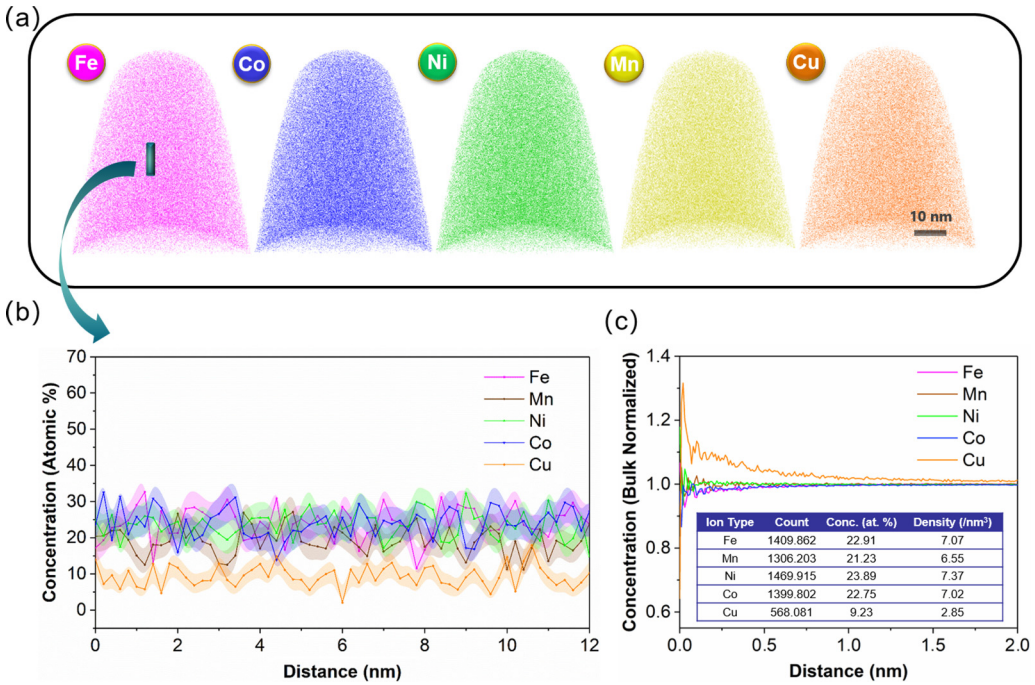

FIG. 9. APT analysis of the homogenized $FeNiCoMnCu_{0.5}$ alloy. (a) 3D APT tip reconstructions of Fe, Ni, Co, Mn, and Cu. (b) 1D compositional profile along the length direction of the cylinder shown in (a). (c) Radial distribution functions of Cu-Fe, -Co, -Ni, -Mn, and -Cu representing the radial concentration profile of all the elements starting from each detected Cu atom. The radial concentration profile in (c) shows the probability density of finding an atom at 2 nm spacing when a Cu atom is placed at the origin [52,53] and 0.2 nm was taken as the step size as well as the shell thickness.

measured concentration at each position was normalized with respect to the average bulk concentration. In the profile of Fig. 9(c), Cu has higher value than 1 which means that Cu is prone to stay closer to Cu, while Fe and Co both have values below 1, showing that they are repelled by Cu.

We further conducted APT analysis of the homogenized FeNiCoMnCu alloy. Figure 10(a) shows the three-dimensional (3D) distribution of Fe, Co, and Cu and the 2D reconstruction of platelike Cu enriched zones. Inhomogeneity of Fe, Co, and Cu can be clearly observed. In contrast, Ni and

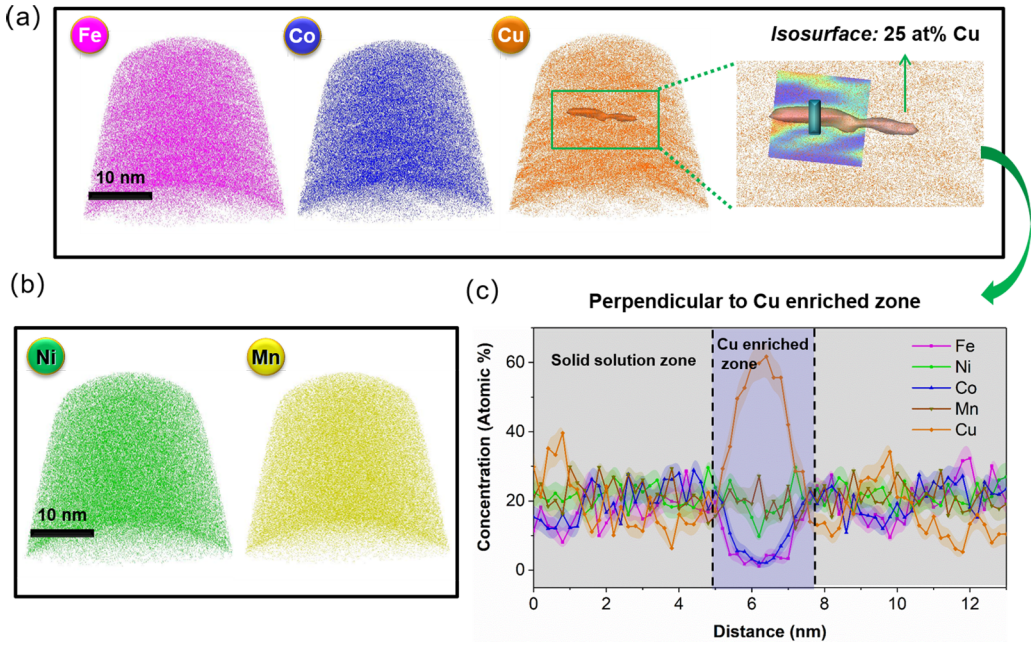

FIG. 10. APT analysis of the homogenized FeNiCoMnCu alloy. (a) 3D distribution of Fe, Co, and Cu and 2D reconstruction of platelike Cu enriched zones. (b) 3D APT tip reconstructions of Ni and Mn. (c) 1D compositional profile taken along the length direction of the cylinder shown in the 2D reconstruction of platelike Cu enriched zones in (a).

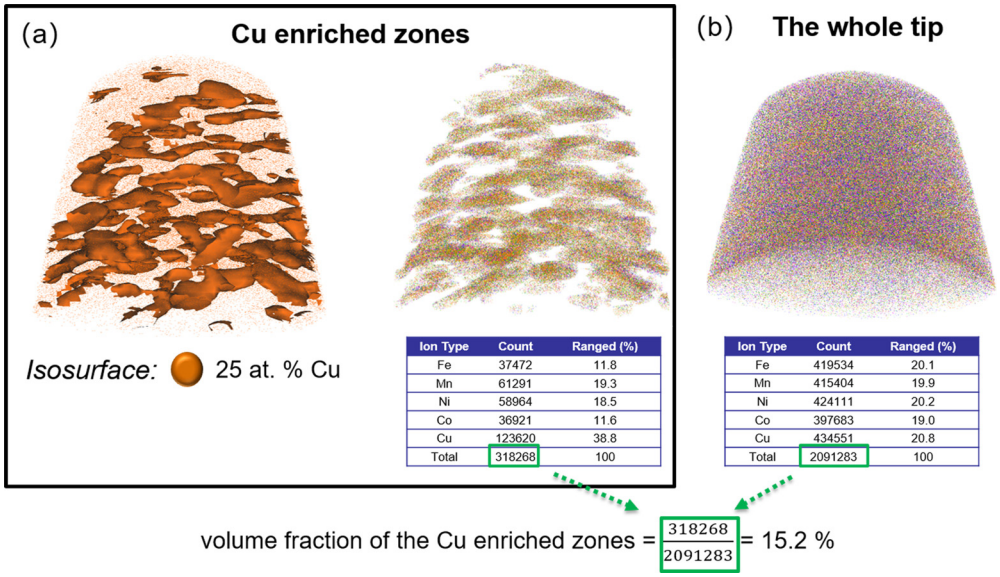

FIG. 11. (a) 25 at. % isoconcentration surface of Cu and corresponding atom map for all the elements in the Cu enriched zones. (b) Atom map of all the elements in the whole tip. The volume fraction of Cu enriched zones is around 15.2% calculated by the total ion counts in the Cu enriched zones divided by the total ion counts in the whole tip.

Mn are uniformly distributed in Fig. 10(b). Figure 10(c) shows the corresponding 1D compositional profile taken along the length direction of the cylinder marked in Fig. 10(a). Cu enriched zones with approximately 2 nm in width can be clearly observed. The concentration of Cu even reaches a maximum value of 60% while Fe and Co are depleted in these zones. The formation of Cu enriched zones is related to the large positive mixing enthalpy of Fe-Cu and Co-Cu binary systems as mentioned above. Figure 11(a) shows the 25 at. % isoconcentration surface of Cu and the corresponding atom map for all the elements in the Cu enriched zones. The tables in Figs. 11(a) and 11(b) show the ion counts and ranged compositions of all elements in the Cu enriched zones for the entire tip. The volume fraction of the Cu enriched zones is ∼15.2%.

The APT data show that the elements in the homogenized FeNiCoMn alloy without Cu are uniformly distributed at the nanoscale. In the homogenized $FeNiCoMnCu_{0.5}$ alloy we find slight elemental fluctuations, but no obvious segregation or decomposition. The homogenized FeNiCoMnCu alloy contains nanosized Cu enriched zones with a volume fraction of ∼15.2%. This analysis thus reveals that an increase in Cu promotes a trend for elemental decomposition.

On the property side we observed that the Curie temperature increases (Fig. 7) and that the magnetic state transforms from paramagnetism to ferromagnetism at room temperature (Fig. 14(b) in the Appendix) with the addition of Cu in the homogenized alloys. This means that the Cu addition and the formation of the Cu enriched zones and the depleted regions around it in the homogenized FeNiCoMnCu alloy must be responsible for the changes in magnetic behavior. To understand the origin of this effect, we performed *ab initio* calculations as discussed below.

C. Origin of anomalous magnetic properties analyzed by *ab initio* calculation

In the calculations, we have considered homogeneous mixing of atoms for all the three alloys within the CPA approach. This simulation scenario reflects ideal solid solutions and is thus not applicable to the as-cast samples. Magnetism for related calculations has been in most previous works treated employing a ferrimagnetic (Ferri) and a paramagnetic (PM) state [28,43,44], which can both be computationally very efficiently modelled based on a one-atomic (primitive) cell. However, at lower temperatures, the constitutive elements Fe and Mn are known to often prefer an antiferromagnetic ordering in fccbulk [54,55]. To account for such possible magnetic states, we employed in the present work a conventional four-atom fccunit cell. This allows us, in contrast to most previous CPA-based works for HEAs, to consider various antiferromagnetic orderings. We considered in total five different magnetic states, namely, ferromagnetic (FM), ferrimagnetic (Ferri), antiferromagnetic 1 (AFM1), antiferromagnetic 2 (AFM2), and paramagnetic (PM) state in the present study (see Fig. 16 for schematics of magnetic states). In particular the two prominent AFM states show particular stability at low temperatures as will be discussed below.

Figure 12 shows the total energy as a function of lattice constant for different magnetic states of FeNiCoMn, $FeNiCoMnCu_{0.5}$, and FeNiCoMnCu HEAs calculated at 0 K. For all the alloys, a magenta arrow marks the lattice constant below which all Mn spins change orientation from ferromagnetic alignment (FM state) to antiferromagnetic alignment (Ferri state) with respect to Fe and Co spins. It can also be seen that the lattice constant for spin flip and the energy difference between the Ferri and the FM states around the spin-flip region decreases with increasing Cu content. This signifies the sensitivity of Mn spin orientation with respect to volume and chemical environment. Nevertheless, our calculations reveal that none of these states is the preferred magnetic state. The AFM1 state with Mn atoms having a layered antiferromagnetic arrangement of spins is the lowest energy magnetic state for all three alloys. Interestingly, for the FeNiCoMn alloy, the AFM2 state with layered antiferromagnetic arrangement of Fe

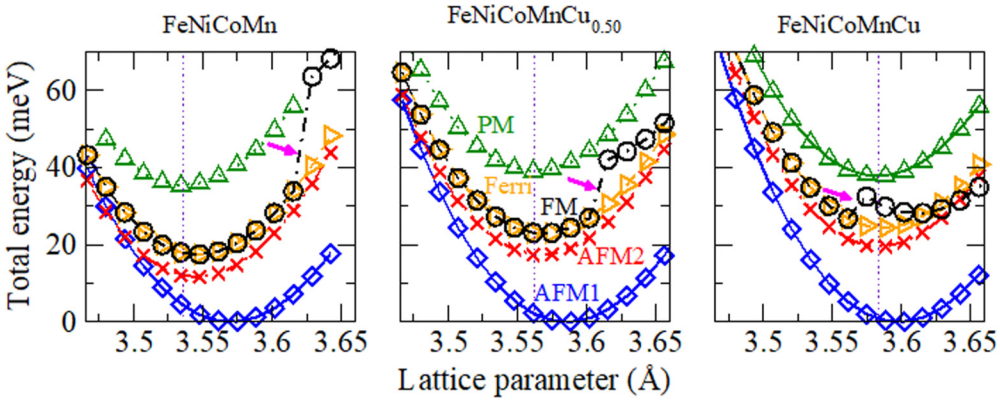

FIG. 12. Total energy as a function of lattice constant for the five magnetic states of FeNiCoMn, FeNiCoMnCu$_{0.5}$, and FeNiCoMnCu HEAs at 0 K. The magenta arrow indicates the lattice constant below which the FM state transforms into the Ferri state.

and Mn spins is strongly stabilized and for lattice constants below 3.49 Å it represents the most stable magnetic state. For Cu containing alloys, the AFM1 state, however, clearly represents the lowest energy magnetic state in a wide range of lattice constants. This indicates that Cu plays a pivotal role in the stabilization of a ferromagnetic ordering of Fe in the here investigated HEAs. The relative stability of the AFM1 state with respect to the AFM2 state is also confirmed by supercell-based calculations (see the Appendix, subsec. 4, for details). This stabilization of the ferromagnetic Fe ordering has a significant impact on magnetic properties, such as Curie temperatures, as we will discuss below.

We next focus on the magnetic properties and investigate the origin of the anomalous increase in T_C due to Cu addition. The T_C values are estimated based on a mean-field approximation [21,56] as

$$T_C = \frac{1}{k_B}\frac{2}{3(1-c)}(E_{PM} - E_{AFM1}), \quad (1)$$

where E_{AFM1} and E_{PM} are the energies of the AFM1 and PM states respectively at the optimized lattice parameter of the PM state, k_B is the Boltzmann constant, and c is the concentration of nonmagnetic element in the alloy. Our calculated T_C values, as listed in Table IV, increase continuously with increasing Cu content. This trend agrees well with the experimental observation for the homogenized alloys shown in Fig. 7. As an often-observed feature, the mean-field approximation provides qualitatively correct trends for the prediction of T_C, but overestimates the absolute values of T_C, which is also evident from the comparison between the calculated and the experimentally measured T_C for all the homogenized alloys in Fig. 7. It should also be mentioned that the consideration of the Ferri state instead of the AFM1 state in the estimation of the T_C would have resulted in a qualitatively opposite trend in the T_C. This highlights the significance of the AFM1 state considered in the present work.

Due to the addition of Cu, the alloys undergo two key changes. First, the lattice parameter of the alloys increases as observed in experiments and supported by the corresponding theoretical calculations (Table IV). In addition, the concentration of magnetic elements in the alloys also decreases. Unraveling the fundamental mechanism of the abnormal changes in T_C requires disentangling the effect of these twofold changes caused by the Cu addition. In order to demonstrate the effect of the lattice parameter or volume expansion we next calculate T_C as a function of lattice parameter for FeNiCoMn and FeNiCoMnCu$_{0.5}$. Figure 13 shows that the T_C for both alloys increases monotonically with increasing lattice parameter. We also find that the T_C of FeNiCoMn at the lattice parameter of FeNiCoMnCu$_{0.5}$ (3.562 Å) increases by approximately 49 K as compared to the value at its own equilibrium lattice parameter (3.536 Å). This indicates that the volume expansion, which is an elastic effect, can partially explain the 76.3-K (approximately) increment in T_C from FeNiCoMn to FeNiCoMnCu$_{0.5}$ (filled green and red symbols respectively in Fig. 13). The remaining part (i.e., 27.3 K) of the enhanced T_C can thus be attributed to the changes in chemical composition of the four magnetic elements (i.e., Fe, Ni, Co, and Mn) due

TABLE IV. Experimentally measured (homogenized alloy) and theoretically calculated (PM) lattice parameters for all the three alloys. Curie temperatures T_C are computed at the lattice parameters of the PM state while the saturation magnetizations are determined at 0 K for the two considered AFM states (see Fig. 16 in the Appendix for definition).

	Lattice parameter (Å)			Saturation magnetization At 0 K (A m^2/kg)	
Alloy	measured (homogenized)	calculated (PM state)	T_C (K) calculated	calculated (AFM1 state)	calculated (AFM2 state)
FeNiCoMn	3.5890	3.536	242.0	96.1	26.7
FeNiCoMnCu$_{0.5}$	3.6127	3.562	318.3	89.7	25.9
FeNiCoMnCu	3.6200	3.583	357.7	80.8	23.7

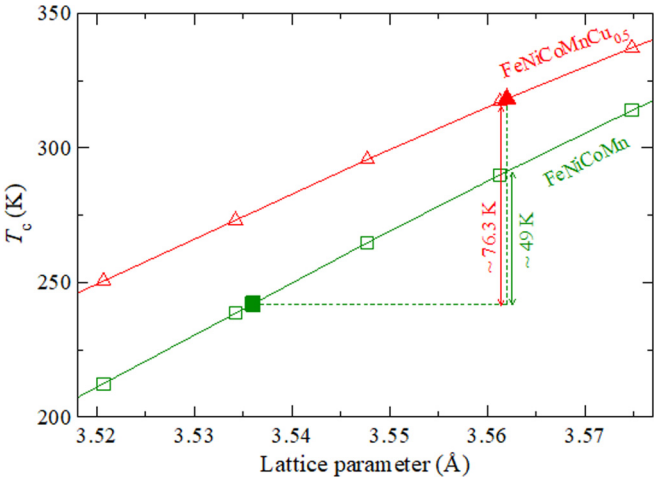

FIG. 13. Curie temperature T_C as a function of lattice parameter for FeNiCoMn (green symbols) and FeNiCoMnCu$_{0.5}$ (red symbols) estimated based on a mean-field approximation. The filled symbols indicate T_C of these two alloys at their respective optimized lattice parameters in the PM state.

to Cu substitution. Hence the fundamental mechanism of the increase in T_C of FeNiCoMn alloy due to Cu substitution lies in the combined change of the unit cell volume and the chemical composition of the alloy.

The experimental data also show an increase in magnetization due to Cu addition [Fig. 6(a)]. To further investigate this effect, we employ first-principles calculations to determine the ground-state saturation magnetization at 0 K. Considering AFM1 as the lowest energy magnetic state at 0 K, we present in Table IV the calculated values of the saturation magnetization in this state for the three alloys. Because of the proximity of the AFM1 and AFM2 magnetic states in the energy landscape, in particular for the FeNiCoMn reference alloy, we also present magnetization values for the AFM2 state in the table. It can be seen that among the two Cu containing alloys, FeNiCoMnCu$_{0.5}$ has larger saturation magnetization at 0 K. This is in agreement with low temperature experimental results as shown in Fig. 6(a). For the Cu free alloy, the calculated saturation magnetization, however, shows a different trend than the measured values. Among the three alloys, FeNiCoMn exhibits the lowest saturation magnetization in experimental measurements while our calculations indicate the highest magnetization for this alloy. It should however be noted that for the FeNiCoMn alloy, the AFM2 state lies very close in energy to the AFM1 state with the former being the lowest energy state for lattice constants below 3.49 Å (see Fig. 12). We therefore speculate that a mixture of both magnetic states, likely corresponding to a very complex magnetic ground state, could exist in this alloy. Since the magnetization of the AFM2 state is almost 2/7 as that of the AFM1 state, such a magnetic state would likely have significantly lower magnetization being more close to the experimental findings. A further analysis would, however, require larger simulation cells, which is beyond the scope of the present work. For most practical applications the magnetization values close to room temperature are, however, more relevant. And, as shown in Fig. 6(b), independent of the chosen reference state (AFM1 or AFM2), the Curie temperature for FeNiCoMn would be in any case significantly below room temperature. This is also in agreement with our measurements in which only a negligible room temperature magnetization is found for FeNiCoMn.

In order to assess the finite-temperature behavior we resort to the semiempirical Kuz'min formula [47,48] given as

$$M(\tau) = M_0[1 - s\tau^{\frac{3}{2}} - (1-s)\tau^p]^{1/3}, \qquad (2)$$

where M_0 is the saturation magnetization at 0 K, s and p are empirical parameters which have been chosen as 0.11 and 2.5, respectively, and τ is equal to T/T_C. The s and p parameters cannot straightforwardly be obtained by DFT simulations and we therefore have taken reported values for pure Co [47]. The so calculated results for the magnetization as a function of temperature are shown in Fig. 6(b). It can be seen that for both, the AFM1 and AFM2 states close to room temperature, FeNiCoMn has the lowest magnetization with almost negligible value. This is a consequence of the lower T_C value because of which the decrease of magnetization for FeNiCoMn is fastest among the three alloys. On the other hand, FeNiCoMnCu has the highest magnetization at room temperature with FeCoNiMnCu$_{0.5}$ having an intermediate value. Interestingly, this trend of magnetization in Cu containing alloys is completely opposite to that at 0 K where FeNiCoMnCu has lower saturation magnetization. As shown in Fig. 6(b), a crossing of the magnetization curves for the two Cu containing alloys occurs at a temperature around 262 K. A qualitatively similar crossing of the magnetization curves is also observed in experiments albeit at a slightly lower temperature [Fig. 6(a)]. The origin of this behavior of magnetization lies in the difference in T_C among the two alloys. Hence, our calculations suggest the highest and lowest magnetizations at room temperature for FeNiCoMnCu and FeNiCoMn alloys, respectively, with FeCoNiMnCu$_{0.5}$ having an intermediate value. This qualitatively explains the experimentally observed trend of an increase in magnetization at room temperature due to the Cu addition.

As mentioned in the experimental parts, there are still some Cu enriched zones in the homogenized FeNiCoMnCu alloy. To further corroborate our findings, we incorporated the effect of the different compositions of these zones into the calculation of the magnetization. From the APT analysis, the volume fraction of nanosized Cu enriched zones is around 15.2%, and the average composition of these zones is around $Fe_{11.8}Ni_{18.5}Co_{11.6}Mn_{19.3}Cu_{38.8}$. By *ab initio* calculations we found that the Curie temperature and 0-K saturation magnetization of such Cu enriched zones are 284.2 K and 47.5 A m^2/kg, respectively. Within a very first approximation we carried out a linearly weighted summation of both zones and find that the saturation magnetization at 0 K and Curie temperature for the homogenized FeNiCoMnCu alloy were 75.7 A m^2/kg and 346.5 K, respectively. These values are slightly lower than those obtained without considering the Cu enriched zones (Table IV). This first-order approximation indicates that the Cu enriched zones tend to slightly reduce the magnetization and Curie temperature.

V. CONCLUSIONS

This work is an investigation of the effects of Cu additions to the FeNiCoMn HEA system. For this purpose FeNiCoMn, $FeNiCoMnCu_{0.5}$, and FeNiCoMnCu HEAs have been prepared by bulk metallurgical casting, rolling, and homogenization heat treatment processing. Chemical, microstructural, and magnetic characterization have been combined with DFT-based calculations to unveil the abnormal magnetic behavior observed in these alloys caused by Cu addition. The main conclusions are as follows:

(1) The as-cast alloys show dendritic microstructures. The dendrite regions are enriched with Fe and Co, while Mn, Ni, and Cu are enriched in the interdendrite regions. In homogenized condition, all elements in the FeNiCoMn HEA are uniformly distributed in a single-phase fccstructure. For the other Cu containing HEAs, Cu is slightly repelled by Fe and Co when mapped at the nanoscale, while Mn and Ni are uniformly distributed.

(2) For as-cast HEAs, saturation magnetization at room temperature increases by 77% and 177% for Cu concentrations of 11 and 20 at. %, respectively, compared to the equiatomic reference FeNiCoMn material without Cu addition. For homogenized HEAs, the magnetic state at room temperature transforms from paramagnetism to ferromagnetism at 20 at. % Cu addition.

(3) The difference in magnetic properties between the homogenized and the as-cast alloys is due to the formation of a Fe-Co enriched phase in the dendritic regions of the as-cast alloys. Further, as-cast alloys with higher Cu content show a higher degree of chemical decomposition and hence higher saturation magnetization.

(4) The homogenized FeNiCoMnCu alloy contains nano-sized Cu enriched zones with a volume fraction of ∼15.2% according to APT analysis. The Cu enriched zones slightly reduce the magnetization and Curie temperature.

(5) *Ab initio* calculations indicate that Cu plays a pivotal role in the stabilization of ferromagnetic ordering of Fe. The calculated magnetization and Curie temperatures of the three alloys agree qualitatively well with the experimental results. A combined change in volume and chemical composition as revealed by theoretical calculations explains the abnormal magnetic behavior caused by Cu addition.

(6) This study suggests that inexpensive nonmagnetic elements, e.g., Cu can be utilized to tune the Curie temperature and saturation magnetization in the HEAs.

ACKNOWLEDGMENTS

Funding from the Deutsche Forschungsgemeinschaft (SPP 2006) and from NWO/STW (VIDI Grant No. 15707) are gratefully acknowledged. Z.R. would like to acknowledge the financial support from the China Scholarship Council (Grant No. 201706460026). Z.L. would like to acknowledge the final support from the National Science Foundation of China (Grant No. 51971248) and the Hunan Special Funding for the Construction of Innovative Province (Grant No. 2019RS1001). The kind support of B. Breitbach, F. Schlüter, M. Nellessen, K. Angenendt, and P. Siegmund at the Max-Planck-Institut für Eisenforschung is gratefully acknowledged.

APPENDIX

1. Hysteresis loops

Figure 14 shows the hysteresis loops of the as-cast and homogenized FeNiCoMn, $FeNiCoMnCu_{0.5}$, and FeNiCoMnCu HEAs. The values of saturation magnetization at room temperature listed in Table III for the three alloys are determined from these magnetization measurements.

2. Temperature dependencies of magnetization curves

Figure 15 shows the demagnetization behavior of the as-cast and homogenized FeNiCoMn, $FeNiCoMnCu_{0.5}$, and FeNiCoMnCu HEAs. The corresponding Curie temperatures estimated by the derivative of the M-T curves are listed in Table III.

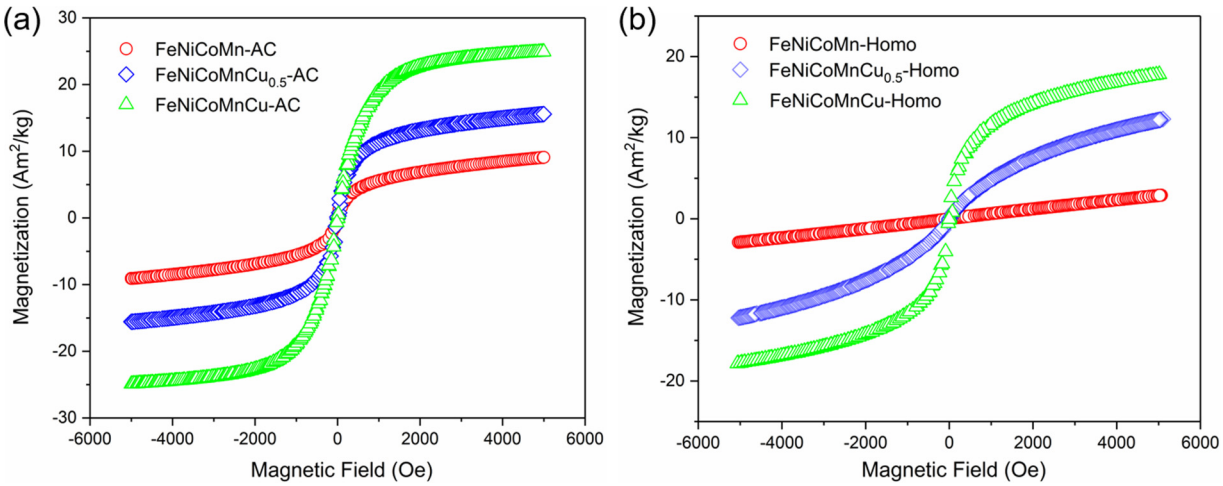

FIG. 14. Hysteresis loops investigated up to 0.5 T at room temperature of (a) as-cast (AC) and (b) homogenized (homo.) FeNiCoMn, $FeNiCoMnCu_{0.5}$, and FeNiCoMnCu HEAs. The volume magnetization is plotted as magnetic moment in units of A m^2/kg.

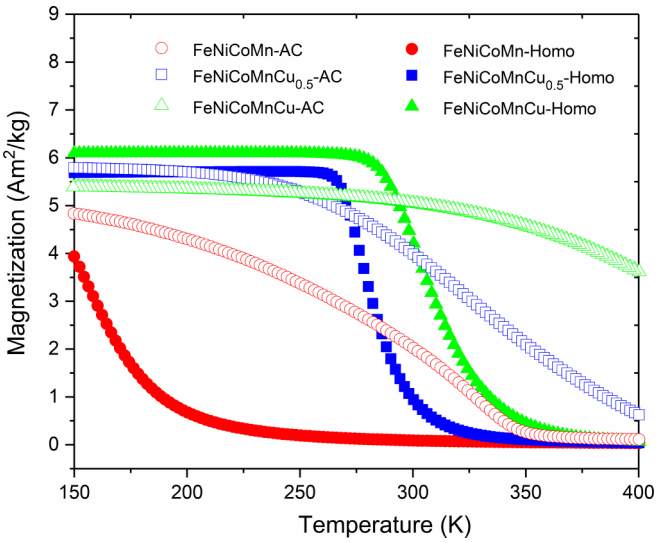

FIG. 15. Temperature dependence of magnetization of as-cast (AC) and homogenized (homo.) FeNiCoMn, $FeNiCoMnCu_{0.5}$, FeNiCoMnCu HEAs at 0.01 T in vacuum.

3. Schematics

Figure 16 shows schematics of five different magnetic states considered for each of the alloys. All the states are named according to the relative alignment of Mn, Fe, and Co spins. Ni (Cu) spins are not shown in the figure because of their relatively smaller (negligible) magnitude of magnetic moments as compared to Fe, Co, and Mn. In the ferromagnetic (FM) state, all spins of the three elements are aligned in the same direction. The scenario is changed in the ferrimagnetic (Ferri) state where Mn atoms have opposite spins to that of Fe and Co. In the antiferromagnetic 1 (AFM1) state Mn atoms are arranged in alternating layers having up and down spins respectively with all Fe and Co spins aligned only in one direction. For the antiferromagnetic 2 (AFM2) state, both Mn and Fe atoms have layered antiferromagnetic arrangement of spins while Co spins remain aligned in one direction like the AFM1 state. Finally, in the paramagnetic (PM) state, which becomes stable above T_C, all atoms have equal amounts of up and down spins mixed at each lattice site (DLM approach) so that the net magnetization of the system is zero.

4. Comparison between EMTO-CPA and VASP-supercell computed results

In order to further validate the results obtained using the EMTO-CPA approach, we additionally calculated total energies of the two antiferromagnetic states AFM1 and AFM2 using the supercell approach and compared the results obtained using both theoretical methods. Calculations using supercells were performed using DFT utilizing plane-wave basis set as implemented in the Vienna Ab-Initio Simulation Package

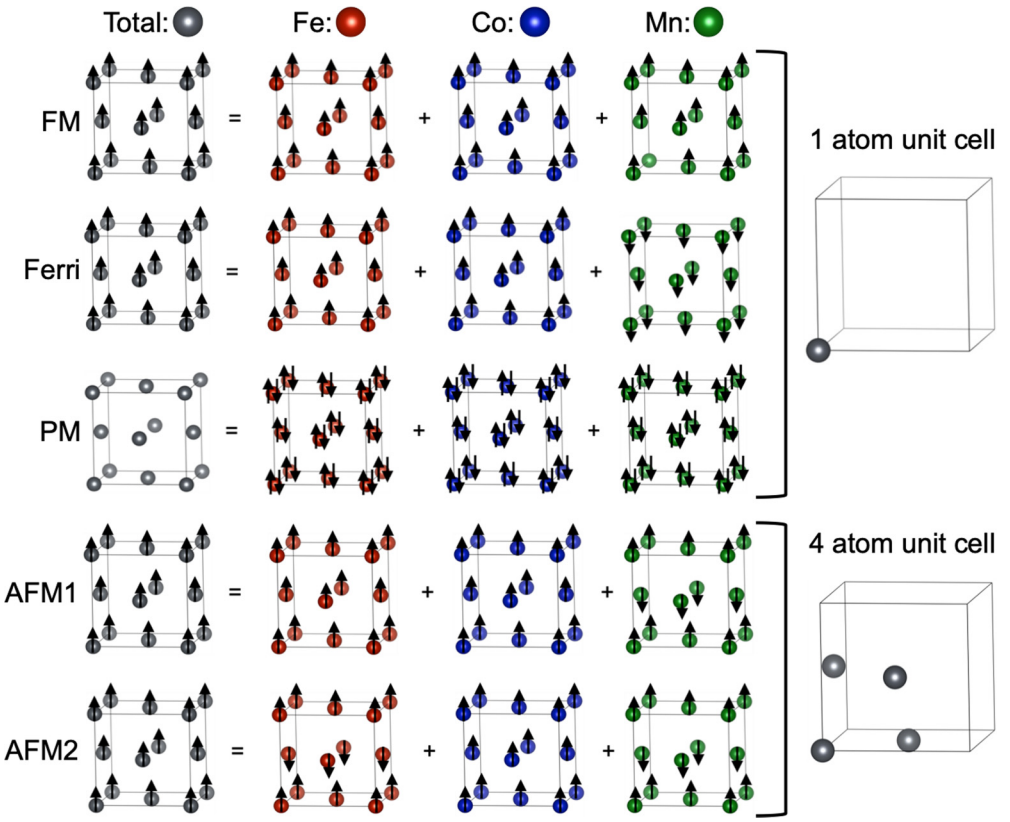

FIG. 16. Schematic models of ferromagnetic (FM), ferrimagnetic (Ferri), antiferromagnetic 1 (AFM1), antiferromagnetic 2 (AFM2), and disordered local moment (DLM) paramagnetic (PM) states of FeNiCoMn, $FeNiCoMnCu_{0.5}$, and FeNiCoMnCu HEAs used in *ab initio* calculations. The black arrows indicate the direction of spins. The FM, Ferri, and PM states can be modeled with one atom unit cell while modeling the AFM1 and AFM2 states requires minimum four atoms as indicated above.

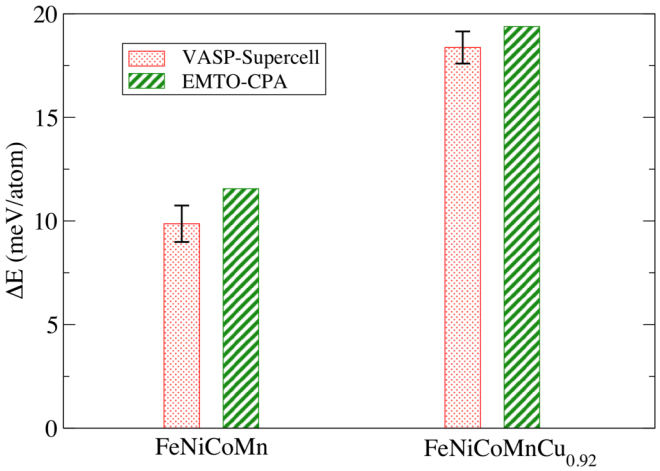

FIG. 17. Difference in total energy (ΔE) at 0 K between the two antiferromagnetic states AFM1 and AFM2 calculated using VASP-supercell (red bar) and EMTO-CPA (green bar) methods for FeNiCoMn and $FeNiCoMnCu_{0.92}$ alloys. The error bar for VASP-supercell computed result indicates the standard error of the mean obtained by averaging over eight different SQS calculations.

(VASP) [57,58]. The projector augmented wave (PAW) method [59], together with the GGA [39] for the exchange-correlation potential, was used for the calculation of total energies. A large basis with a plane-wave cutoff of 450 eV and k-point grid of $8 \times 8 \times 4$ was employed in the present calculations. In order to model randomly disordered configurations of alloys, we generated several 64-atom special quasirandom structures (SQSs) [60] using the ATAT package [61]. To obtain a sufficient statistical sampling over the chosen configurations, the calculated results were averaged over eight different SQSs for each magnetic state.

A comparison of the results using the two theoretical methods for the Cu-free alloy (i.e., FeNiCoMn) and a Cu containing alloy (i.e., $FeNiCoMnCu_{0.92}$) is presented in Fig. 17. For the Cu containing alloy, the chosen composition is the closest to the equiatomic FeNiCoMnCu which can be modelled with a 64-atom SQS. The figure shows the energy difference (ΔE) between the total energy minima of the AFM1 and AFM2 states. The results with the supercell approach are obtained by averaging over the energy differences for eight SQSs and the corresponding error bar indicates the standard statistical error of the mean. As shown in the figure, the energy difference obtained with the two theoretical methods agrees very well for both alloys. The trend of increased energy difference with increasing Cu content is also captured by both methods. These results further corroborate the applicability of the computationally efficient EMTO-CPA method for capturing the energetics of different magnetic states in these alloys.

We note that the stabilization of other magnetic states, particularly the Ferri and the PM states in supercell-based calculations, can be extremely challenging as also pointed out in previous works [62]. Our findings indicate however that in cases where no convergence issues are present, the supercell approach agrees well with the EMTO-CPA approach. The difficulty associated with the treatment of different magnetic states in the supercell approach further emphasizes the advantage of the EMTO-CPA method for the present study.

[1] B. Cantor, I. Chang, P. Knight, and A. Vincent, Mater. Sci. Eng. A **375-377**, 213 (2004).

[2] J. W. Yeh, S. K. Chen, S. J. Lin, J. Y. Gan, T. S. Chin, T. T. Shun, C. H. Tsau, and S. Y. Chang, Adv. Eng. Mater. **6**, 299 (2004).

[3] J. W. Yeh, S. Y. Chang, Y. D. Hong, S. K. Chen, and S. J. Lin, Mater. Chem. Phys. **103**, 41 (2007).

[4] Y. P. Wang, B. S. Li, and H. Z. Fu, Adv. Eng. Mater. **11**, 641 (2009).

[5] F. Otto, A. Dlouhý, C. Somsen, H. Bei, G. Eggeler, and E. P. George, Acta Mater. **61**, 5743 (2013).

[6] B. Gludovatz, A. Hohenwarter, D. Catoor, E. H. Chang, E. P. George, and R. O. Ritchie, Science **345**, 1153 (2014).

[7] M. Yao, K. G. Pradeep, C. C. Tasan, and D. Raabe, Scr. Mater. **72-73**, 5 (2014).

[8] Y. Zhang, T. T. Zuo, Z. Tang, M. C. Gao, K. A. Dahmen, P. K. Liaw, and Z. P. Lu, Prog. Mater. Sci. **61**, 1 (2014).

[9] Z. Li, K. G. Pradeep, Y. Deng, D. Raabe, and C. C. Tasan, Nature (London) **534**, 227 (2016).

[10] Y. Yao, Z. Huang, P. Xie, S. D. Lacey, R. J. Jacob, H. Xie, F. Chen, A. Nie, T. Pu, M. Rehwoldt, D. Yu, M. R. Zachariah, C. Wang, R. Shahbazian-Yassar, J. Li, and L. Hu, Science **359**, 1489 (2018).

[11] Z. Lei, X. Liu, Y. Wu, H. Wang, S. Jiang, S. Wang, X. Hui, Y. Wu, B. Gault, P. Kontis, D. Raabe, L. Gu, Q. Zhang, H. Chen, H. Wang, J. Liu, K. An, Q. Zeng, T. G. Nieh, and Z. Lu, Nature (London) **563**, 546 (2018).

[12] Y. Deng, C. C. Tasan, K. G. Pradeep, H. Springer, A. Kostka, and D. Raabe, Acta Mater. **94**, 124 (2015).

[13] H. Huang, Y. Wu, J. He, H. Wang, X. Liu, K. An, W. Wu, and Z. Lu, Adv. Mater. **29**, 1701678 (2017).

[14] Z. Li, C. C. Tasan, K. G. Pradeep, and D. Raabe, Acta Mater. **131**, 323 (2017).

[15] S. Nene, K. Liu, M. Frank, R. Mishra, R. Brennan, K. Cho, Z. Li, and D. Raabe, Sci. Rep. **7**, 16167 (2017).

[16] Z. Li, Acta Mater. **164**, 400 (2019).

[17] E. P. George, D. Raabe, and R. O. Ritchie, Nat. Rev. Mater. **4**, 515 (2019).

[18] S. Singh, N. Wanderka, K. Kiefer, K. Siemensmeyer, and J. Banhart, Ultramicroscopy **111**, 619 (2011).

[19] Y. Zhang, T. Zuo, Y. Cheng, and P. K. Liaw, Sci. Rep. **3**, 1455 (2013).

[20] P. Koželj, S. Vrtnik, A. Jelen, S. Jazbec, Z. Jagličić, S. Maiti, M. Feuerbacher, W. Steurer, and J. Dolinšek, Phys. Rev. Lett. **113**, 107001 (2014).

[21] F. Körmann, D. Ma, D. D. Belyea, M. S. Lucas, C. W. Miller, B. Grabowski, and M. H. Sluiter, Appl. Phys. Lett. **107**, 142404 (2015).

[22] O. Schneeweiss, M. Friák, M. Dudová, D. Holec, M. Šob, D. Kriegner, V. Holý, P. Beran, E. P. George, J. Neugebauer, and A. Dlouhý, Phys. Rev. B **96**, 014437 (2017).

[23] Y. Yuan, Y. Wu, X. Tong, H. Zhang, H. Wang, X. Liu, L. Ma, H. Suo, and Z. Lu, Acta Mater. **125**, 481 (2017).

[24] M. C. Gao, D. B. Miracle, D. Maurice, X. Yan, Y. Zhang, and J. A. Hawk, J Mater. Res. **33**, 3138 (2018).

[25] G. Laplanche, P. Gadaud, C. Bärsch, K. Demtröder, C. Reinhart, J. Schreuer, and E. P. George, J Alloys Compd. **746**, 244 (2018).

[26] Z. Rao, D. Ponge, F. Körmann, Y. Ikeda, O. Schneeweiss, M. Friák, J. Neugebauer, D. Raabe, and Z. Li, Intermetallics **111**, 106520 (2019).

[27] Q. Zhang, H. Xu, X. Tan, X. Hou, S. Wu, G. Tan, and L. Yu, J Alloys Compd. **693**, 1061 (2017).

[28] S. Huang, E. Holmström, O. Eriksson, and L. Vitos, Intermetallics **95**, 80 (2018).

[29] S. Huang, W. Li, X. Li, S. Schönecker, L. Bergqvist, E. Holmström, L. K. Varga, and L. Vitos, Mater. Des. **103**, 71 (2016).

[30] C. L. Chien, S. H. Liou, D. Kofalt, W. Yu, T. Egami, T. J. Watson, and T. R. McGuire, Phys. Rev. B **33**, 3247 (1986).

[31] R. M. Bozorth, *Ferromagnetism* (Wiley-VCH, Hoboken, 1993), p. 992.

[32] E. Ma, M. Atzmon, and F. Pinkerton, J. Appl. Phys. **74**, 955 (1993).

[33] Z. Li and D. Raabe, JOM **69**, 2099 (2017).

[34] O. Dmitrieva, D. Ponge, G. Inden, J. Millán, P. Choi, J. Sietsma, and D. Raabe, Acta Mater. **59**, 364 (2011).

[35] M. Herbig, P. Choi, and D. Raabe, Ultramicroscopy **153**, 32 (2015).

[36] M. Herbig, D. Raabe, Y. J. Li, P. Choi, S. Zaefferer, and S. Goto, Phys. Rev. Lett. **112**, 126103 (2014).

[37] L. Vitos, Comput. Mater. Sci. **18**, 24 (2000).

[38] L. Vitos, Phys. Rev. B **64**, 014107 (2001).

[39] J. P. Perdew, K. Burke, and M. Ernzerhof, Phys. Rev. Lett. **77**, 3865 (1996).

[40] P. Soven, Phys. Rev. **156**, 809 (1967).

[41] B. L. Gyorffy, A. J. Pindor, J. Staunton, G. M. Stocks, and H. Winter, J. Phys. F: Met. Phys. **15**, 1337 (1985).

[42] H. J. Monkhorst and J. D. Pack, Phys. Rev. B **13**, 5188 (1976).

[43] D. Ma, B. Grabowski, F. Körmann, J. Neugebauer, and D. Raabe, Acta Mater. **100**, 90 (2015).

[44] X. Sun, H. Zhang, S. Lu, X. Ding, Y. Wang, and L. Vitos, Acta Mater. **140**, 366 (2017).

[45] Z. Rao, X. Wang, J. Zhu, X. Chen, L. Wang, J. Si, Y. Wu, and X. Hui, Intermetallics **77**, 23 (2016).

[46] F. Otto, Y. Yang, H. Bei, and E. P. George, Acta Mater. **61**, 2628 (2013).

[47] M. D. Kuz'min, Phys. Rev. Lett. **94**, 107204 (2005).

[48] M. D. Kuz'min, M. Richter, and A. N. Yaresko, Phys. Rev. B **73**, 100401(R) (2006).

[49] M. Okada, G. Thomas, M. Homma, and H. Kaneko, IEEE T. Magn. **14**, 245 (1978).

[50] Y. F. Kao, S. K. Chen, T. J. Chen, P. C. Chu, J. W. Yeh, and S. J. Lin, J Alloys Compd. **509**, 1607 (2011).

[51] B. Gault, M. P. Moody, J. M. Cairney, and S. P. Ringer, *Atom Probe Microscopy* (Springer Science & Business Media, New York, 2012), Vol. 160.

[52] M. Miller and E. Kenik, Microsc. Microanal. **10**, 336 (2004).

[53] F. De Geuser, W. Lefebvre, and D. Blavette, Philos. Mag. Lett. **86**, 227 (2006).

[54] W. Pepperhoff and M. Acet, *Constitution and Magnetism of Iron and its Alloys* (Springer Science & Business Media, Berlin Heidelberg, 2013).

[55] P. Bobadova-Parvanova, K. A. Jackson, S. Srinivas, and M. Horoi, Phys. Rev. A **67**, 061202(R) (2003).

[56] K. Sato, L. Bergqvist, J. Kudrnovský, P. H. Dederichs, O. Eriksson, I. Turek, B. Sanyal, G. Bouzerar, H. Katayama-Yoshida, V. A. Dinh, T. Fukushima, H. Kizaki, and R. Zeller, Rev. Mod. Phys. **82**, 1633 (2010).

[57] G. Kresse and J. Hafner, Phys. Rev. B **47**, 558 (1993).

[58] G. Kresse and J. Furthmüller, Phys. Rev. B **54**, 11169 (1996).

[59] P. E. Blöchl, Phys. Rev. B **50**, 17953 (1994).

[60] A. Zunger, S.-H. Wei, L. G. Ferreira, and J. E. Bernard, Phys. Rev. Lett. **65**, 353 (1990).

[61] A. van de Walle and G. Ceder, J. Phase Equilib. **23**, 348 (2002).

[62] H. Song, F. Tian, Q.-M. Hu, L. Vitos, Y. Wang, J. Shen, and N. Chen, Phys. Rev. Mater. **1**, 023404 (2017).